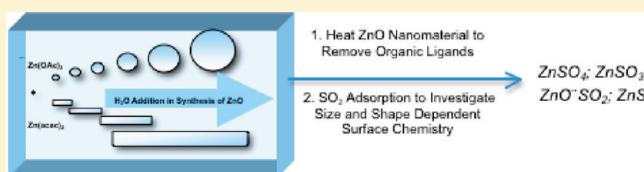


Sulfur Dioxide Adsorption on ZnO Nanoparticles and Nanorods

Chia-Ming Wu, Jonas Baltrusaitis, Edward G. Gillan, and Vicki H. Grassian*

Department of Chemistry, University of Iowa, Iowa City, Iowa 52246, United States

ABSTRACT: ZnO nanomaterials, nanoparticles, and nanorods, have been synthesized over a wide range of sizes with relatively high yield (~90–95%). The synthesis method allows for size control by varying the amount of water used and morphology control by varying the zinc precursor (zinc acetate for nanoparticles or zinc acetylacetonate for nanorods). These nanomaterials were analyzed with powder X-ray diffraction and attenuated total reflection FTIR spectroscopy. Sulfur dioxide adsorption on nanoparticles and nanorods of different size was then investigated using volumetric measurements, transmission FTIR spectroscopy, and X-ray photoelectron spectroscopy. Nanoparticles and nanorods of several different sizes were heated to 550 °C to remove surface-adsorbed organic ligands that remained after the synthesis prior to exposure to SO₂. Spectroscopic analysis revealed the formation of several surface species, including sulfate, sulfite, sulfide, and weakly bound SO₂. Quantifying surface speciation as well as the total amount of adsorbed sulfur from XPS and volumetric data reveals that sulfur speciation as well as the total amount of adsorbed sulfur is a function of particle size and morphology.



INTRODUCTION

Zinc oxide is a semiconductor material ($E_g = 3.37$ eV) with a free exciton binding energy of ~60 meV¹ and is commonly used as a chemical sensor,^{2,3} phosphor,^{4,5} photocatalyst,^{6–8} and photovoltaic device.^{9,10} The synthesis of zinc oxide nanomaterials has received a great deal of attention due to the interest in its size-dependent properties and applications.^{11,12}

Several different synthetic strategies have been employed for zinc oxide nanocrystals with different morphologies, including sol–gel processes,^{13,14} wet chemical methods,^{15–17} chemical vapor deposition,^{4,18} and spray pyrolysis.^{19,20} Many of these methods involve multistep procedures, long reaction times, and/or use of toxic solvents or reactants. Furthermore, although many studies focus on the production of zinc oxide nanomaterials, only few focus on the synthesis of gram quantities of nanomaterials that can be prepared with different sizes, relatively narrow size distributions, and different morphologies. Large quantities are useful from a scale-up production standpoint and in applications of catalysis and as adsorbents. Large quantities of nanomaterials of variable size are also needed to investigate the environmental health and safety of nanomaterials, an active and ongoing area of research,²¹ and can be used as standards for the development of analytical methods to detect nanomaterials in complex milieu such as in the environment and in biological system.²²

Here we present a synthetic approach that uses water as the variable to control particle size. In addition, different zinc salt precursors give rise to different ZnO morphologies—spherical particles versus rods. The advantages of this approach include short reaction times of 1 h or less, size control over a relatively large size range, and a high yield (95%). Furthermore, this method is surfactant-free and has the potential to be environmentally friendly and produce relatively large quantities (grams) of the nanomaterials.²¹

Surface properties as well as bulk properties of synthesized ZnO nanomaterials are characterized in this study due to the

importance of surface functionality on the behavior of nanomaterials. Phase and morphology were characterized using powder X-ray diffraction (XRD) and transmission electron microscopy (TEM). Surface area was analyzed using BET and chemical composition was followed by XPS, while chemical functionality was investigated using attenuated total reflection–Fourier transform infrared (ATR-FTIR).

In addition, using these well-characterized synthesized nanomaterials, we have investigated the adsorption of sulfur dioxide on ZnO. Sulfur dioxide adsorption on ZnO is of interest as it is a major air pollutant generated from combustion of fossil fuel or volcano eruption. SO₂ can also poison metal and metal oxide catalysts in various industrial processes as well as ZnO-based gas sensors.²³ Sulfur species are commonly removed from feed streams by ZnO adsorbents in order to preserve downstream catalytic activity.²⁴ Thus, there is great interest in the adsorption of sulfur dioxide on ZnO nanomaterials.²⁵ Here we discuss the adsorption properties of SO₂ on ZnO nanomaterials as a function of size and shape using spectroscopic and quantitative adsorption measurements.

EXPERIMENTAL METHODS

Synthesis of Spherical ZnO Nanoparticles. ZnO nanoparticle synthesis employed a wet chemical method, shown in Figure 1. First, 1.98 g (9 mmol) of zinc acetate dihydrate (Alfa Aesar, >98%) was added to 40 mL of methanol. The solution was then refluxed for several minutes. Various amounts of water (1–25 mL) were then added to this solution. After water addition, 30 mL of a methanol solution containing 0.72 g (18 mmol) of NaOH was

Received: March 1, 2011

Revised: April 8, 2011

Published: May 02, 2011

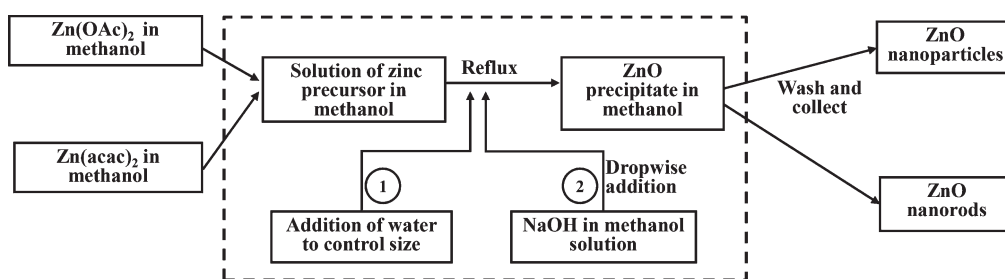


Figure 1. Synthetic scheme used to prepare powdered samples of spherical ZnO nanoparticles and ZnO nanorod of different size by controlling the addition of water in the synthesis. See text for further details.

added dropwise to the resulting solution. After 30 minutes of reaction at reflux temperatures, a white precipitate was collected by centrifugation. For reactions with water additions of 15 mL or greater, refluxing was continued for an additional 30 min prior to product isolation to improve particle homogeneity. The isolated precipitates were washed three times using a 1:1 ratio of ethanol/acetone and dried under vacuum for 1 day. The weight of the ZnO product from a 1 mL water addition reaction was 0.69 g, which corresponds to a 95% yield based on the zinc precursor reactant. Reactions with other amounts of water similarly produced ZnO yields in excess of 90%.

Synthesis of ZnO Nanorods. The synthesis of ZnO nanorods is similar to the synthetic method discussed above for ZnO spherically shaped nanoparticles but involves the use of a different zinc precursor. For the synthesis of nanorods, 2.37 g (9 mmol) of zinc acetylacetonate (Acros, ~98%) was dissolved in 40 mL of methanol. The mixture was refluxed for a few minutes to dissolve the precursor. Similar to the nanoparticle method discussed above, various amounts of water (1–10 mL) were then added to the zinc-containing solution under reflux conditions followed by addition of a 30 mL methanol solution containing 0.72 g (18 mmol) of NaOH. After 30 min of refluxing, a white precipitate was collected by centrifugation. The precipitate was washed as discussed above and dried under vacuum for 1 day. The final ZnO product from 1 mL water addition was 0.67 g, which corresponds to a 90% yield based on the Zn precursor reactant. Reactions with other amounts of water similarly produced ZnO yields in excess of 90%.

Nanomaterial Characterization. Several methods and techniques were used to characterize the bulk phase, composition, particle size, particle morphology, surface area, and surface composition of ZnO nanomaterials. For bulk crystalline phase analysis, powder X-ray diffraction (XRD) measurements were employed using a Rigaku MiniFlex II with a filtered cobalt source. Crystallite sizes from XRD were calculated using peak broadening of the (101) reflection and the Scherrer equation. For size and morphology, a JEOL 1230 transmission electron microscope (TEM) was used, and average particle size and dimensions were determined from the analysis of 50–100 particles. Surface areas for different powder samples were measured using the nitrogen adsorption seven-point Brunauer–Emmett–Teller (BET) technique on an automated instrument (Quantachrome NOVA 4200e) in the P/P_0 range from 0.05 to 0.3. The samples were degassed at 80 °C overnight before their surface area measurements were taken. Surface composition of the ZnO nanomaterials was investigated using attenuated total reflectance Fourier transform infrared (ATR-FTIR). Thermogravimetric analysis (TGA) was performed starting from room temperature to 900 °C with a 10 °C min⁻¹ heating rate under flowing

air to quantify the amount volatile compounds removed from ZnO nanomaterials as a function of temperature.

Transmission FTIR Spectroscopy and Quantitative Adsorption Measurements of Sulfur Dioxide on ZnO Nanomaterials. A Mattson Galaxy 6000 infrared spectrometer was employed to measure the transmission FTIR spectroscopy of ZnO nanomaterials following SO₂ adsorption. The infrared cell was also used for volumetric measurements as previously reported.²⁶ Approximately 5 mg of ZnO powder was mounted onto a tungsten mesh and loaded into an IR sample cell and then heated under vacuum to remove adsorbed organic ligands that remained on the surface following the synthesis of these materials. It was determined by transmission Fourier transform infrared spectroscopy (FTIR) that after heating the sample to 550 °C for 2 h the organic ligands could be removed. FTIR spectra of ZnO nanomaterials exposed to SO₂ were acquired at 4 cm⁻¹ resolution and referenced to background scans obtained for the clean ZnO sample prior to SO₂ exposure. Gas-phase SO₂ absorption was subtracted from FTIR spectra reported here. For volumetric measurements, 100 mTorr of SO₂ was introduced into the reaction chamber, and the pressure change of SO₂ in the chamber was recorded after 30 min with and without sample present and converted into the total amount of adsorbed SO₂.

XPS Analysis of Sulfur Dioxide Adsorption on ZnO Nanoparticles and Nanorods. A custom-designed Kratos Axis Ultra X-ray photoelectron spectroscopy system was used in all experiments and has been described in detail before.²⁷ The surface analysis chamber is equipped with aluminum K α X-ray gun and 500 mm Rowland circle silicon single crystal monochromator. The X-ray gun was operated using a 15 mA emission current at an accelerating voltage of 15 kV. Low-energy electrons were used for charge compensation to neutralize the sample. Survey scans were collected using the following instrument parameters: energy scan range of 1200 to -5 eV; pass energy of 160 eV; step size of 1 eV; dwell time of 200 ms, and an X-ray spot size of 700 × 300 μ m. High-resolution spectra were acquired in the region of interest using the following experimental parameters: 20–40 eV energy window; pass energy of 20 eV; step size of 0.1 eV, and dwell time of 1000 ms. One sweep was used to acquire a survey spectrum of all binding regions. The absolute energy scale was calibrated to the Cu 2p_{2/3} peak binding energy of 932.6 eV using an etched copper plate. Following the reaction with SO₂ and FTIR analysis, ZnO powdered samples were pressed into an indium foil and mounted onto a copper stub. These samples were then transferred into XPS instrument for analysis.

Calibration Procedure, Data Processing of Core Photoelectron Spectra, and Reference Materials. All spectra were calibrated using C 1s peak at 285.0 eV. A Shirley-type background was subtracted from each spectrum to account for inelastically scattered electrons that contribute to the broad background. CasaXPS software was used to process the XPS data.²⁸ Transmission corrected relative sensitivity factor (RSF) values, obtained from the Kratos library, were used for quantifying surface composition and the total amount of adsorbed sulfur. The S 2p transition was fit to two peaks with a ratio of 2:1 for the 2p_{3/2} and 2p_{1/2} transitions, respectively. The S 2p doublet was constrained to a separation energy of 1.2 eV with equivalent full width at half-maximum (fwhm). The components of the peaks contain a Gaussian/Lorentzian product with 30% Lorentzian and 70% Gaussian character. An error of ± 0.2 eV is reported for all the peak binding energies. The Monte Carlo error calculation method was used to determine the precision of the calculations,²⁷ as implemented in the CasaXPS software.²⁸

Additionally, several sulfur-containing standard compounds were analyzed with XPS to determine binding energies for the S 2p_{3/2} and S 2p_{1/2} transitions and aid in the analysis of the XPS data following SO₂ adsorption on ZnO nanomaterials. In particular, elemental sulfur (99.999%, Acros Organics), ZnS (99.99% trace metals basis, Aldrich), ZnSO₃ (99%, MP Biomedicals), ZnSO₄·H₂O (99%, Acros Organics), and ZnSO₄·7H₂O (99.999%, Aldrich) powders were used.

RESULTS AND DISCUSSION

Synthesis and Characterization of Spherical ZnO Nanoparticles. As already noted, different amounts of water were added during the hydrolysis step of the synthesis to control particle size. The effect of controlled water addition in the synthesis of ZnO nanomaterials has been previously discussed in several reports.^{13,29,30} It has been suggested that water promotes particle growth due to the increase in the rate of ZnO condensation. Powder XRD patterns of ZnO nanoparticles produced by controlled zinc acetate [Zn(OAc)₂] hydrolysis are shown in Figure 2. The samples in Figure 2 differ in the amount of water added during the reaction and were 1, 3, 5, 7, 10, 15, 20, and 25 mL of water for samples A through H, respectively. The XRD pattern shows the hexagonal wurtzite structure for all of the samples. There is some narrowing of the peaks in the XRD patterns from A to H, indicating that larger ZnO nanocrystals are formed with increasing amount of water in the synthesis. XRD curve A for the ZnO nanoparticles prepared with 1 mL of water shows the broadest peaks which indicate the smallest crystal size. A nanoparticle diameter of 9 nm is calculated using Scherrer's equation (see Table 1).³¹ As can be seen in Table 1, larger crystallite sizes are calculated for nanoparticles prepared with the addition of more water to the synthesis.

Corresponding TEM images of ZnO nanoparticles synthesized from Zn(OAc)₂ are shown in Figure 3. The results obtained from TEM images of samples A through H support the size changes in XRD data. TEM images show the change in nanoparticle size with increasing amounts of water added to the synthesis. These images also show that these ZnO nanoparticles are roughly spherical and have fairly uniform size. Figure 3A shows that the smallest ZnO nanoparticles obtained in this study are 7 ± 2 nm in diameter. Images shown in Figure 3B–H are for larger ZnO particles with average diameters increasing from 17 ± 3 to 130 ± 21 nm, respectively, as increasing amounts of

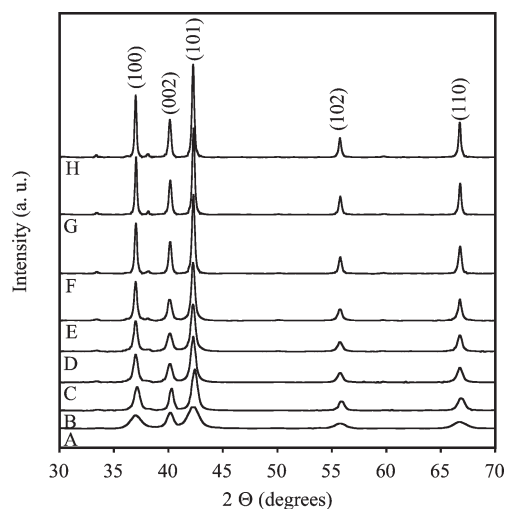


Figure 2. Powder XRD pattern (Co K α radiation) of ZnO nanoparticles synthesized from Zn(OAc)₂ according to the scheme shown in Figure 1. Different amounts of water amount were adjusted in the synthesis as a way to control particle size. The different samples labeled A–H differ in the amount of water added to the reactions as follows: A, 1; B, 3; C, 5; D, 7; E, 10; F, 15; G, 20; and H, 25 mL of H₂O.

Table 1. Summary of XRD, TEM, and BET Results for Spherical ZnO Nanoparticles^a

sample	water added ^b (mL)	XRD crystallite size (nm)	TEM size (nm)	BET surface area (m ² g ^{−1})
A	1	9	7 ± 2	75 ± 4
B	3	18	17 ± 3	50 ± 3
C	5	22	24 ± 3	40 ± 2
D	7	26	29 ± 4	35 ± 2
E	10	35	47 ± 7	26 ± 1
F	15	45	73 ± 12	17 ± 1
G	20	59	98 ± 14	14 ± 1
H	25	61	130 ± 21	11 ± 1

^a Zn(OAc)₂ precursor used. ^b Amount of water added to synthesis to control particle size.

water were used during the synthesis (Table 1). These results indicate that a large range of particle sizes, from 7 ± 2 to 130 ± 21 nm, can be obtained using this method.

The XRD and TEM data for the ZnO nanoparticles produced from Zn(OAc)₂ are summarized in Table 1. A comparison of the crystallite size calculated from the (101) XRD reflection to the TEM data is in quite good agreement for nanoparticles below 30 nm. However, for larger particles, these different methods for calculating size diverge. This is possibly due to the fact that XRD measures crystallite size, and the larger particles may be polycrystalline composed of smaller crystallites that have coalesced to form the larger sized nanoparticles.

The synthesis of ZnO nanomaterials using the method outlined in Figure 1 gives a relatively high yield (>90%). Thermogravimetric analysis (TGA) data show only two minor decreases in sample weight at 200 and 400 °C, corresponding to 2% and 3.2% weight loss, respectively. Thus, only small amounts of surface adsorbed volatiles contribute to the total mass. It is speculated that the weight loss at 200 °C is associated with the water loss from the surface of ZnO and at 400 °C is likely due to

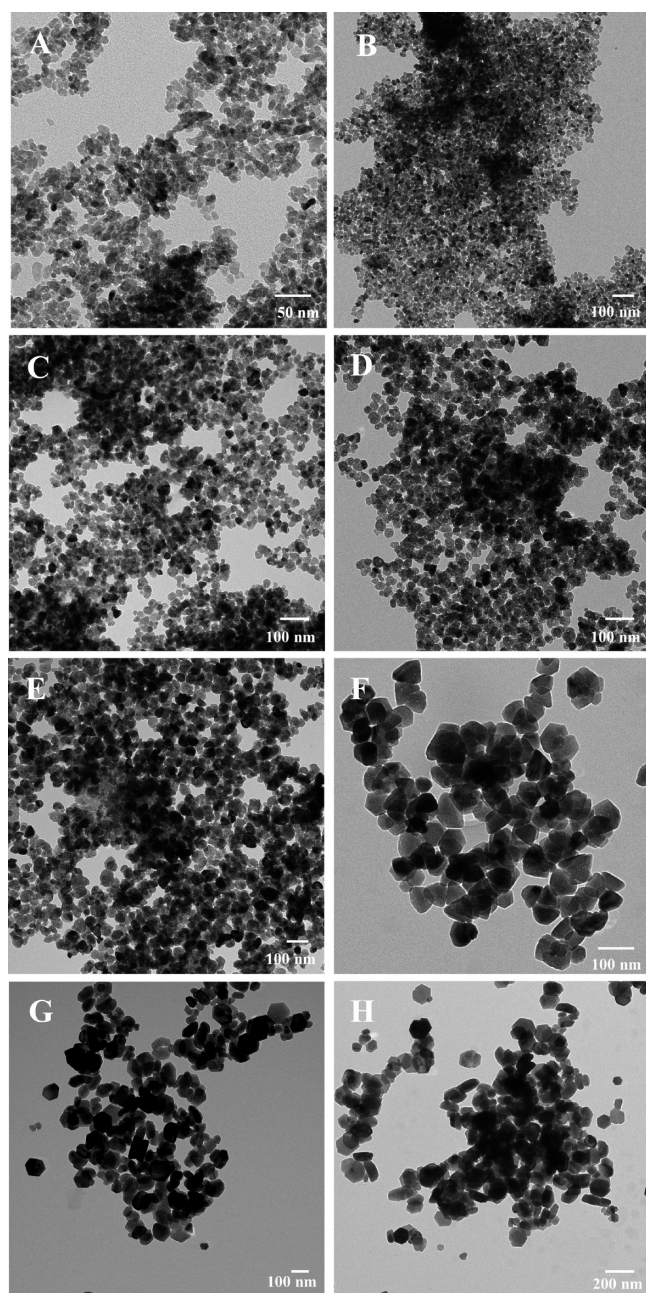


Figure 3. TEM images of ZnO nanoparticles synthesized from $\text{Zn}(\text{OAc})_2$. Similar to that noted in caption for Figure 2, different amounts of water amount were adjusted in the synthesis as a way to control particle size. The different samples labeled A–H differ in the amount of water added to the reactions as follows: A, 1; B, 3; C, 5; D, 7; E, 10; F, 15; G, 20; and H, 25 mL of H_2O .

volatilization and/or decomposition of surface adsorbed ligands derived from the zinc precursor (*vide infra*).

Synthesis and Characterization of ZnO Nanorods. The synthesis of ZnO nanomaterials from zinc acetylacetonate [$\text{Zn}(\text{acac})_2$] instead of $\text{Zn}(\text{OAc})_2$, following the same procedure outlined in Figure 1, results in a change in morphology. ZnO nanorods synthesized using $\text{Zn}(\text{acac})_2$ as the precursor give the XRD patterns and TEM images shown in Figures 4 and 5. The samples in Figures 4 and 5 differ in the amount of water added during the reaction and were 1, 3, 5, 7, and 10 mL of water for

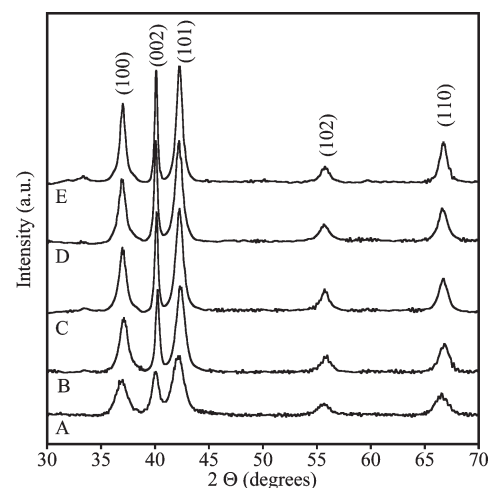


Figure 4. Powder XRD pattern (Co K α radiation) of ZnO nanorods synthesized from $\text{Zn}(\text{acac})_2$ according to the scheme shown in Figure 1. Different amounts of water amount were adjusted in the synthesis as a way to control rod size. The different samples labeled A–E differ in the amount of water added to the reaction as follows: A, 1; B, 3; C, 5; D, 7; and E, 10 mL of H_2O .

samples A through E, respectively. The broadest peaks with a crystal size of 9 nm are for curve A, while curve E shows the largest crystal size of ~ 17 nm. In Table 2, a summary of the XRD and TEM for ZnO nanorods synthesized using $\text{Zn}(\text{acac})_2$ as the precursor is given.

With the exception of sample A, the (002) reflection in the XRD patterns in Figure 4 shows a more pronounced decrease in peak width and an increase in intensity relative to other reflections and indicates a preferred (002) growth orientation in the ZnO nanostructure,³² therefore suggesting a rod structure. In fact, except for sample A, a nanorod morphology of ZnO product is observed in the TEM images shown in Figure 5. The TEM image of Figure 5A shows a spherical nanoparticle with diameter of 7 ± 1 nm, whereas the TEM images in Figure 5B–E show nanorods. It can be seen that the width of the nanorods for samples B–E increases from 14 ± 2 to 41 ± 6 nm, respectively, and the length increases from 46 ± 8 to 325 ± 50 nm, respectively (see Table 2). These changes result in an increase in the aspect ratio from three to eight as the nanorods grow to larger size. These XRD and TEM results imply either preferred growth along the length of the rod and/or that acac ligands may cap rod walls more strongly relative to the ends of the rods. Further evidence for the latter model could be obtained from molecular dynamics simulations as these provide information on ligand–surface interactions and their role in controlling the shape of oxide nanomaterials.³³

Surface Analysis of ZnO Spherical Nanoparticles and Nanorods Produced from $\text{Zn}(\text{OAc})_2$ and $\text{Zn}(\text{acac})_2$ Precursors. As the ZnO nanoparticles and nanorods grow in size, they have lower BET-measured surface areas as expected (Tables 1 and 2). For example, the BET surface area of spherical ZnO nanoparticles is seen to decrease from 75 ± 4 to 11 ± 1 m^2/g , as the particle size increased as a result of an increase in the amount of water used in the synthesis. The standard deviations of the BET surface area measurements reported in Tables 1 and 2 are determined to be less than or near 5% from multiple measurements. Calculated geometric surface areas for the larger nanoparticles were in good agreement with the BET measured surface areas. However, calculated geometric areas for the smaller

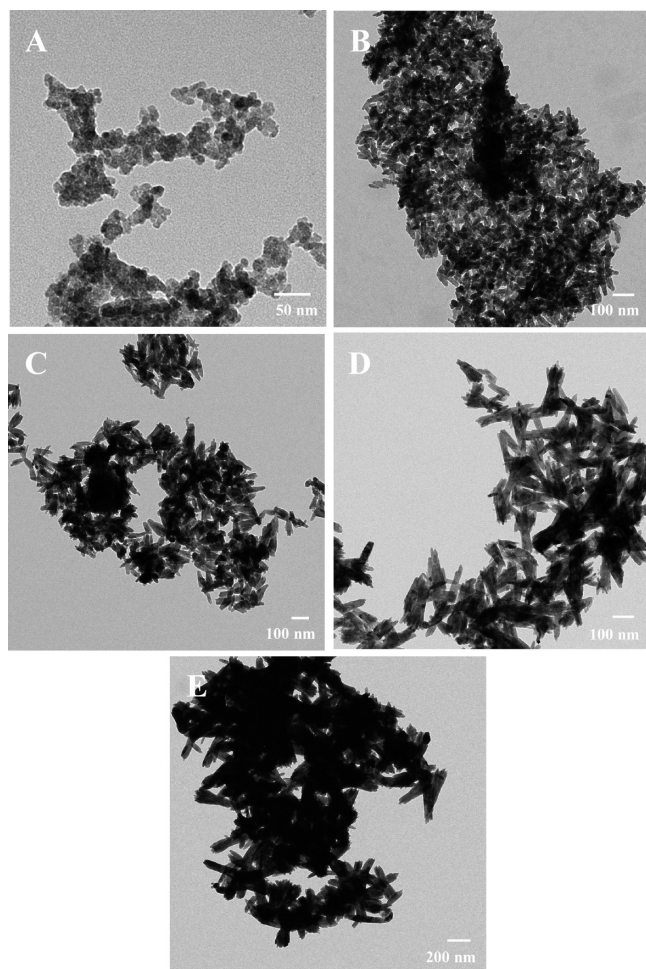


Figure 5. TEM images of ZnO nanorods synthesized from $\text{Zn}(\text{acac})_2$. Different amounts of water amount were adjusted in the synthesis as a way to control particle size. The different samples labeled A–E differ in the amount of water added to the reaction as follows: A, 1; B, 3; C, 5; D, 7; and E, 10 mL of H_2O .

Table 2. Summary of XRD, TEM, and BET Results for ZnO Nanorods^a

sample	water added ^b (mL)	XRD crystallite size (nm)	TEM size (nm), width (W), length (L)	BET surface area ($\text{m}^2 \text{g}^{-1}$)
A ^c	1	9	7 ± 1^c	91 ± 5
B	3	11	W: 14 ± 2 L: 46 ± 8	49 ± 3
C	5	13	W: 16 ± 3 L: 77 ± 10	34 ± 2
D	7	13	W: 22 ± 5 L: 125 ± 17	26 ± 1
E	10	17	W: 41 ± 6 L: 325 ± 50	14 ± 1

^a $\text{Zn}(\text{acac})_2$ precursor used. ^bAmount of water added to synthesis to control size. ^cSample A is more of spherical morphology than rod morphology.

nanoparticles were larger than the measured BET surface areas by more than a factor of 2. It is surmised that the lower than

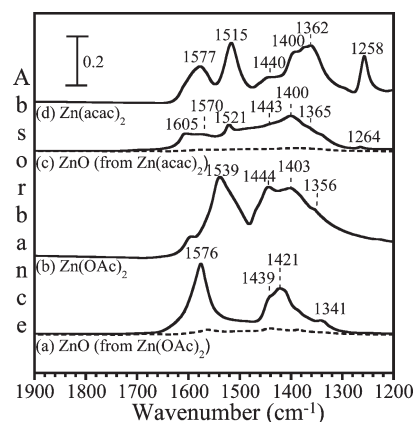


Figure 6. ATR-FTIR spectra acquired in the $1200\text{--}1900 \text{ cm}^{-1}$ region for (a) $7 \pm 2 \text{ nm}$ ZnO from $\text{Zn}(\text{OAc})_2$, (b) $\text{Zn}(\text{OAc})_2$ precursor, (c) $7 \pm 1 \text{ nm}$ ZnO from $\text{Zn}(\text{acac})_2$ and (d) $\text{Zn}(\text{acac})_2$ precursor. Dotted lines show ATR-FTIR spectra of same ZnO nanoparticles after washing with ethanol to remove the organic ligand.

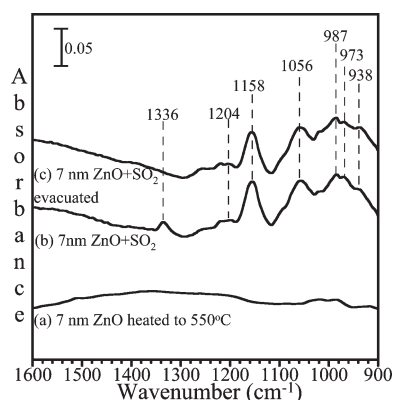


Figure 7. Transmission FTIR spectra of $7 \pm 2 \text{ nm}$ ZnO particles (a) after heating to 550°C for 2 h followed by (b) exposure to 100 mTorr of SO_2 and after (c) evacuation of gas phase SO_2 .

expected surface area occurs for the smaller nanoparticles and nanorods due to aggregation. ZnO nanoparticles and nanorods of smaller size may easily aggregate to reduce their surface energy. Furthermore, for the smaller nanoparticles, the surface area decreased over time by ca. 10%. This result has been reported previously and is due to the instability of ZnO nanoparticles under ambient conditions and their inherent ability to fuse/grow in the presence of atmospheric gases including water vapor, gas-phase CO_2 , and O_2 .³⁴

Additional information about the nature of the surface and the surface composition of ZnO nanomaterials synthesized via the two different precursors was obtained using ATR-FTIR spectroscopy. This technique can provide information about surface functional groups present on the surface and thus a useful description of surface speciation. ATR-FTIR spectra are shown in Figure 6 for the two precursors used in the synthesis, $\text{Zn}(\text{OAc})_2$ and $\text{Zn}(\text{acac})_2$, as well as ZnO nanoparticles synthesized using each of these precursors.

The ATR-FTIR spectra shown in Figure 6a,b are those of the $7 \pm 2 \text{ nm}$ ZnO nanoparticles synthesized using $\text{Zn}(\text{OAc})_2$ as a precursor and the $\text{Zn}(\text{OAc})_2$ precursor, respectively. For the ZnO nanoparticles shown in Figure 6a there are two intense

Table 3. Vibrational Assignments and Vibrational Frequencies (in cm^{-1}) of Adsorbed Sulfur Species ZnO Nanoparticles

adsorbed sulfur species	frequencies (this study)	frequencies (ref)
physisorbed SO_2	1336	1330 (Berben et al. ³⁹)
monodentate sulfite (SO_3^{2-})	973, 938	976, 940 (Thompson et al. ⁴⁰)
monodentate sulfate (SO_4^{2-})	1158, 1056, 987	1143, 1044, 970 (Nakamoto et al. ⁴¹)
bidentate sulfate (SO_4^{2-})	1204	1205 (Thompson et al. ⁴⁰)

peaks at 1576 and 1421 cm^{-1} with a shoulder at 1439 cm^{-1} observed in the spectrum. A weaker peak at 1341 cm^{-1} is also present. The frequencies of these absorptions are close to those observed for the asymmetric and symmetric COO stretching motions at 1539 and 1444 cm^{-1} for the $\text{Zn}(\text{OAc})_2$ precursor. Additionally, the $\text{Zn}(\text{OAc})_2$ spectrum are two absorptions at 1403 and 1356 cm^{-1} associated with CH_3 bending modes. These absorption bands are consistent with those reported in the literature for $\text{Zn}(\text{OAc})_2$,³⁵ and the similarity between the two ATR-FTIR spectra shown in Figure 6a,b suggests the presence of acetate groups adsorbed onto the surface of the ZnO nanoparticles.

ATR-FTIR spectra of 7 ± 1 nm ZnO nanorods synthesized using $\text{Zn}(\text{acac})_2$ precursor and of the $\text{Zn}(\text{acac})_2$ precursor are shown in parts c and d of Figure 6, respectively. The ZnO nanorod spectrum shown in Figure 6c exhibits absorption peaks at 1605, 1521, 1400, and 1264 cm^{-1} with shoulders around 1570, 1433, and 1365 cm^{-1} which are shifted but close to the $\text{Zn}(\text{acac})_2$ absorptions observed at 1577, 1515, 1440, 1400, 1362, and 1258 cm^{-1} with shoulders at 1410 and 1460 cm^{-1} . Absorptions near 1515 and 1655 cm^{-1} have been previously assigned to stretching vibrations of C–H and the coupling of the stretching vibrations of C–O and C=C groups adsorbed on ZnO synthesized using $\text{Zn}(\text{acac})_2$.³⁶ More specifically for $\text{Zn}(\text{acac})_2$, characteristic absorptions at 1560, 1515, and 1460 cm^{-1} are assigned to combinations of C–C and C–O stretching modes, the peak at 1410 cm^{-1} to bending modes of CH_3 , and those at 1290 and 1190 cm^{-1} to combinations of stretching of C– CH_3 , C–C, and bending of C–H.^{37,38} In addition, C–H stretching absorptions between 2800 and 2900 cm^{-1} can be seen in spectra a–d of Figure 6. The IR data show that absorptions due to organic ligands adsorbed to synthesized ZnO from $\text{Zn}(\text{acac})_2$ are shifted with respect to those of pure $\text{Zn}(\text{acac})_2$. This may be due different coordination modes for the adsorbed ligand and/or an indication of some decomposition of the ligands on the surface.

For ZnO particles produced from both precursors, it is seen that the surfaces are coated with an adsorbed organic layer. The intensities of the absorption bands associated with these coatings are seen to decrease after washing the collected powdered samples several times with ethanol, as seen by the dashed lines shown in Figure 6a,c. The adsorbed layer can be heated and removed as indicated by TGA analysis and transmission FTIR spectroscopy prior to sulfur dioxide adsorption (vide infra).

Sulfur Dioxide Adsorption on ZnO Nanomaterials. ZnO nanoparticles and nanorods were heated to 550 °C under vacuum to remove surface functional groups. Transmission FTIR spectroscopy showed a clean surface after heating (Figure 7a). An FTIR spectrum of 7 ± 2 nm ZnO nanoparticles following the introduction of 100 mTorr of SO_2 into the infrared cell is shown in Figure 7b. Several SO_2 adsorption products are identified in the spectral region extending from 900 to 1600 cm^{-1} . In particular, the peak at 1336 cm^{-1} corresponds to weakly adsorbed SO_2 .³⁹ This peak disappears from the spectrum following evacuation of gas

phase SO_2 . Absorption bands at 1204, 1158, 1056, and 987 cm^{-1} are assigned to adsorbed sulfate in different bonding coordination modes.^{40,41} Absorption bands at 973 and 938 cm^{-1} are attributed to monodentate sulfite, SO_3^{2-} , on the ZnO nanoparticle surface.⁴⁰ Tabulated vibrational assignments and vibrational frequencies are given in Table 3. FTIR data for other ZnO nanomaterials synthesized here exposed to 100 mTorr of SO_2 were similar in terms of the absorption band frequencies and the different types of adsorption modes observed. Increased pressures of SO_2 resulted in the same spectrum with the exception of an increase in the intensity of the 1336 cm^{-1} absorption band due to physisorbed SO_2 .⁴²

Quantitative volumetric SO_2 uptake measurements revealed differences in SO_2 adsorption on ZnO nanomaterials of different size and shape. Table 4 shows these data which have been normalized to both sample mass and surface area. The adsorption of SO_2 normalized to the ZnO sample mass decreases from $(4.8 \pm 0.3) \times 10^{-7}$ mol of SO_2 g^{-1} to $(2.8 \pm 0.2) \times 10^{-7}$ mol of SO_2 g^{-1} with increasing of particle size for spherical nanoparticles from 7 ± 2 to 47 ± 7 nm. A similar decrease is observed for nanorods with mass normalized uptake decreasing from $(4.6 \pm 0.3) \times 10^{-7}$ mol of SO_2 g^{-1} to $(2.7 \pm 0.1) \times 10^{-7}$ mol of SO_2 g^{-1} for 14 ± 2 nm \times 46 ± 8 nm sized nanorods to 41 ± 6 nm \times 325 ± 50 nm nanorods. These data show size dependent uptake of SO_2 on ZnO nanomaterials as calculated on a per mass basis. BET surface area normalized coverages for SO_2 adsorption shows an increase from $(3.9 \pm 0.2) \times 10^{14}$ molecules of SO_2 cm^{-2} to $(6.4 \pm 0.5) \times 10^{14}$ molecules of SO_2 cm^{-2} for 7 ± 2 nm compared to 47 ± 7 nm ZnO nanoparticles, respectively. There is greater adsorption capacity for larger nanoparticles when normalized to surface area. A similar trend is observed for nanorods (see Table 4); i.e., nanorods also show an increase in SO_2 coverage per unit area with an increase in ZnO particle size. This observation has also been observed by Stark et al., who showed that MgO nanoparticles of increasing size adsorbed more physisorbed SO_2 per surface area.⁴² It was proposed that more planar surfaces for the larger particles were more favorable for this weak adsorption state.

XPS was then used to further investigate the adsorption of SO_2 on ZnO nanomaterials. To aid in the interpretation of adsorbed sulfur species, literature references^{43–45} as well as several sulfur-containing standards were analyzed in order to measure sulfur binding energies for these reference compounds. As already discussed in the Experimental Methods section, the S 2p region of the photoelectron spectrum consists of two peaks corresponding to the $2p_{3/2}$ and $2p_{1/2}$ transitions with a ratio of 2 to 1, respectively. The core photoelectron spectrum of zinc sulfide, elemental sulfur, zinc sulfite, and zinc sulfate are shown in Figure 8 and summarized in Table 5. The S $2p_{3/2}$ transition for S^{2-} , S, SO_3^{2-} , and SO_4^{2-} ions has been determined to be at 162.0, 164.2, 167.7, and 169.4 eV, respectively. In addition, there are no sulfur species detected by XPS analysis on the surface of any of the ZnO nanomaterials prior to the introduction of SO_2 .

Table 4. Summary of Quantitative Measurements for Sulfur Dioxide Adsorption on ZnO Nanomaterials of Different Size and Shape^a

nanoparticle diameters	volumetric measurements ^{a,b}		XPS measurements ^{c,d}			
	coverage 10 ⁻⁷ mol of SO ₂ g ⁻¹	coverage 10 ¹⁴ molecules of SO ₂ cm ⁻²	SO ₃ ²⁻ :Total S	SO ₄ ²⁻ :Total S	S ²⁻ :Total S	S 2p:Zn 2p
7 ± 2 nm	4.8 ± 0.3	3.9 ± 0.2	0.22	0.09	0.69	0.08 ± 0.01
24 ± 3 nm	3.8 ± 0.2	5.7 ± 0.3	0.23	0.12	0.65	0.08 ± 0.01
47 ± 7 nm	2.8 ± 0.2	6.4 ± 0.5	0.22	0.12	0.66	0.09 ± 0.01
nanorod widths (W) and lengths (L)						
	coverage 10 ⁻⁷ mol of SO ₂ g ⁻¹	coverage 10 ¹⁴ molecules of SO ₂ cm ⁻²	SO ₃ ²⁻ :Total S	SO ₄ ²⁻ :Total S	S ²⁻ :Total S	S 2p:Zn 2p
W: 14 ± 2 nm L: 46 ± 8 nm	4.6 ± 0.3	5.6 ± 0.4	0.15	0.18	0.67	0.11 ± 0.01
W: 16 ± 3 nm L: 77 ± 10 nm	3.3 ± 0.2	5.9 ± 0.4	0.34	0.16	0.50	0.10 ± 0.01
W: 41 ± 6 nm L: 325 ± 50 nm	2.7 ± 0.1	11.0 ± 0.5	0.36	0.08	0.56	0.10 ± 0.01

^a ZnO samples were heated at 550 °C for 2 h before volumetric measurements were at 25 °C. ^b Tabulated volumetric coverages are determined from the average and standard deviation of triplicate measurements and are reported as both per mass (mol g⁻¹) and per surface area (molecules cm⁻²). See text for further details. ^c Samples used for volumetric measurements were transferred to the XPS system for further analysis. ^d Errors reported for the S 2p:Zn 2p ratios are calculated using Monte Carlo error analysis. See text for further details.

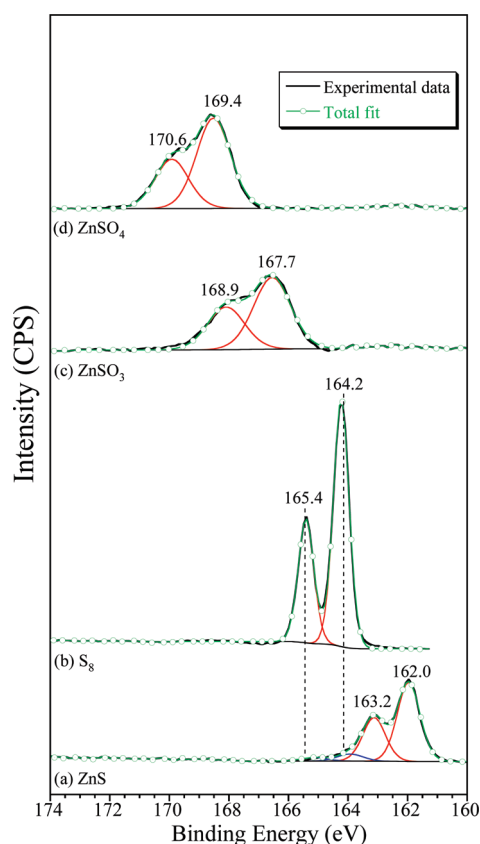
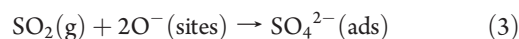
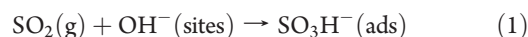


Figure 8. XPS high-resolution S 2p binding energy region for (a) ZnS, (b) elemental sulfur S₈, (c) ZnSO₃, and (d) ZnSO₄. A small amount of S₈ (~5%) was included when fitting the ZnS spectrum.

After establishing these reference binding energies, high-resolution scans of SO₂ exposed nanomaterials in the S 2p region for ZnO nanoparticles and nanorods of various sizes were acquired. These

high-resolution XPS data are shown in Figure 9 (ZnO nanoparticles, left panel; ZnO nanorods, right panel). There are three distinct sulfur transitions observed for ZnO nanomaterials following exposure to SO₂ with S 2p_{3/2} peaks near 162.3, 167.4, and 168.8 eV. The higher binding energy peaks are closest to those observed for adsorbed sulfite and sulfate, respectively, in agreement with FTIR results for surface speciation. While adsorbed sulfite generally results from the interactions of SO₂ with OH⁻ and O²⁻ (eqs and 2), sulfate formation with no light is a result of SO₂ coordination to two oxygen sites (eq 3):²⁷



According to the reference spectra shown in Figure 8, the binding energy of S 2p_{3/2} peak at 162.3 eV is closest to Zn-S rather than elemental S₈ or polymeric sulfur. SO₂ adsorption on Zn metal has been reported to result in formation of chemisorbed sulfur with a transition near ~162.4 eV,²⁵ which is attributed to the dissociative adsorption of sulfur dioxide. The binding energy peak at 162.3 eV observed in the experiments reported here is also assigned to sulfur chemisorbed via strong bond to Zn atoms and can be associated with the decomposition of SO₂. The change in color of the ZnO powder from white to a light yellow following SO₂ adsorption also suggests decomposition of SO₂ on these nanoparticles and nanorods that have been heated to 550 °C in vacuum prior to sulfur dioxide adsorption.

The mechanism for formation of the adsorbed species associated with the peak at 162.3 eV involves S=O bond breaking and is most likely caused by defect formation on the ZnO surface from sample heating at 550 °C to remove adsorbed organic ligands. The Zn:O ratio after heating was close to the stoichiometric value showing there is no metallization leading to zinc formation during heating. The reaction of SO₂ on these ZnO nanomaterials can be envisioned as a two step process with

Table 5. Standard Reference Values for S 2p_{3/2} and S 2p_{1/2} Transitions for Several Sulfur-Containing Compounds

reference compound (sulfur oxidation state)		binding energy, eV	
		this work ^a	literature reference ^b
2p _{3/2}	ZnS (−2)	162.0	161.9 ZnS ⁴⁴
2p _{1/2}		163.2	
2p _{3/2}	S ₈ (0)	164.2	164.2 elemental sulfur (S ₈) ⁴⁵
2p _{1/2}		165.4	
2p _{3/2}	ZnSO ₃ (+4)	167.7	166.7 Na ₂ SO ₃ ; ⁴³ 167.0 CaSO ₃ ; ²⁷ 167.8 on TiO ₂ ²⁷
2p _{1/2}		168.9	
2p _{3/2}	ZnSO ₄ (+6)	169.4	168.9 Na ₂ SO ₄ ; ⁴³ 169.3 Fe ₂ (SO ₄) ₃ ; ⁴³ 169.0 Al ₂ (SO ₄) ⁴³
2p _{1/2}		170.6	

^a Calibrated to the C 1s peak at 285.0 eV. ^b Literature references are given for the S 2p_{3/2} transition, the most intense transition. ZnS referenced to adventitious carbon in Brion et al.;⁴⁴ S 2p_{3/2} energy for S₈ in Riga et al.⁴⁵ referenced to C 1s at 284.5 eV; values reported for Na₂SO₃ by Lindberg et al.⁴³ correspond to a weighted mean for the energies of the S2p_{1/2} and S 2p_{3/2} levels, referenced to C 1s at a reference value of 284.6 eV; S 2p_{3/2} energy for CaSO₃ in Baltrusaitis et al.²⁷ was referenced to C 1s at 285.0 eV; S 2p_{3/2} energy in Baltrusaitis et al.²⁷ was referenced to Ti 2p_{3/2} at 459.3 eV.

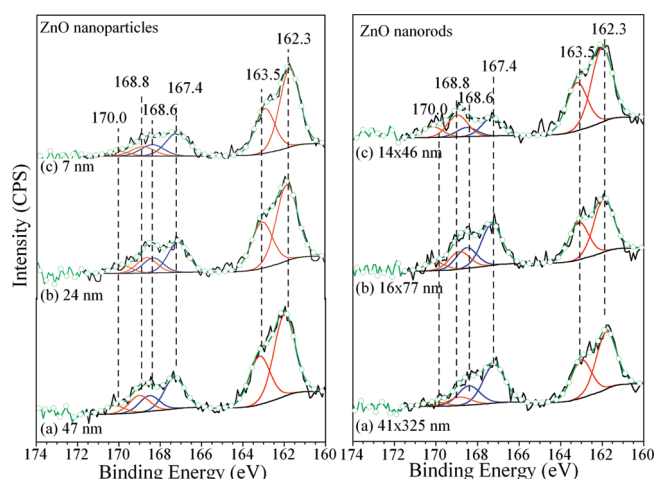


Figure 9. High-resolution S 2p region XPS scans of ZnO nanomaterials of different size and shape following exposure to 100 mTorr of SO₂. Left panel: ZnO nanoparticles (a) 47 ± 7 nm, (b) 24 ± 3 nm, and (c) 7 ± 2 nm. Right panel: ZnO nanorods (a) 41 ± 6 nm × 325 ± 50 nm, (b) 16 ± 3 nm × 77 ± 10 nm, and (c) 14 ± 2 nm × 46 ± 8 nm.

O=S=O bond dissociation with sulfur adsorbing on Zn sites (4,5) and atomic oxygen diffusion to replenish surface oxygen vacancies. Experiments done on samples not heated to 550 °C in vacuum show that although there is still organic ligands on the surface, sulfur dioxide can adsorb but that quantitatively this results in the formation of adsorbed sulfite—as determined by both transmission FTIR spectroscopy and XPS analysis. Sulfite has been observed on ZnO in a recent diffuse reflectance infrared Fourier transform spectroscopy study by Li et al.⁴⁶ Thus, adsorbed sulfide is proposed to form via the dissociation of sulfur dioxide at defect oxygen vacancy sites that are produced during heating.

Quantitative analysis of these different chemisorbed sulfur-containing species following SO₂ exposure is determined by integrating the different peaks. These data are given in Table 4 and reported relative to the total amount of sulfur on the surface (i.e. SO₄^{2−}: Total S; SO₃^{2−}: Total S and S^{2−}: Total S). The S 2p: Zn 2p ratio can be used to quantify the total amount of sulfur on the surface. Unlike volumetric measurements which measure both physisorbed and chemisorbed sulfur species, XPS

quantification is for chemisorbed sulfur species which includes adsorbed sulfate, sulfite, and sulfide. These data show that for nanoparticles and nanorods there are only small differences (ca. 10%) in the total amount of chemisorbed SO₂ as a function of size for a given shape. However, nanorods appear to adsorb 30% more than nanoparticles for the smaller sizes examined. The nanorods also have a greater amount of difference in speciation as a function of size with the smallest rods exhibiting the greatest amount of adsorbed sulfide on the surface. This suggests potentially a greater defect site density for the smallest nanorods, but for the nanoparticles the data suggest the defect site density is independent of size. This is a similar conclusion derived by studies of Barteau and co-workers for TiO₂ nanoparticles.^{47–49} Additionally, particle size due to coarsening as a result of heating to remove surface organics may play a role in the behavior of these nanomaterials and their surface chemistry with sulfur dioxide.

CONCLUSIONS

ZnO nanoparticles and nanorods have been synthesized using a relatively simple synthetic method that allows for size tunability over a wide range of sizes. It is a particularly useful synthesis when gram quantities are desired, such as for use as catalysts and adsorbents or in comparison and interlaboratory studies of the environmental health and safety of nanomaterials or in the development of analytical methods for the detection of nanomaterials in air, water, and soil. Here we focused on using these nanomaterials to better understand sulfur dioxide adsorption. Adsorption of SO₂ on ZnO nanomaterials is found to be size and shape dependent. Quantitative adsorption measurements of SO₂ were performed in addition to spectroscopic analyses. Larger ZnO nanomaterials of the same shape tend to have increased capacity for weakly adsorbed SO₂ on a per surface area basis that is seen in volumetric measurements. ZnO nanorods adsorb more SO₂ per unit surface area compared to nanoparticles. There are at least four different sulfur species forming on these samples that had been heated in vacuum. These sulfur species include sulfate, sulfite, sulfide, and weakly adsorbed sulfur dioxide. The total amount of strongly adsorbing species (sulfate, sulfite, and sulfide) is not size dependent for the nanomaterials investigated, suggesting these may have similar site densities for adsorption.

ACKNOWLEDGMENT

Although the research described in this article has been funded in part (the synthesis of these materials) by the Environmental Protection Agency through Grant EPA R83389101-0 to V.H.G., it has not been subjected to the Agency's required peer and policy review and therefore does not necessarily reflect the views of the Agency, and no official endorsement should be inferred. Additionally, this material (SO₂ uptake on ZnO nanomaterials) is based upon work supported by the National Science Foundation under Grant No. CHB 09526.

REFERENCES

- (1) Polarz, S.; Roy, A.; Merz, M.; Halm, S.; Schröder, D.; Schneider, L.; Bacher, G.; Kruis, F. E.; Driess, M. *Small* **2005**, *1*, 540–552.
- (2) Masuda, Y.; Kato, K. *Cryst. Growth Des.* **2008**, *8*, 275–279.
- (3) Zhang, Y.; Yu, K.; Jiang, D.; Zhu, Z.; Geng, H.; Luo, L. *Appl. Surf. Sci.* **2005**, *242*, 212–217.
- (4) Cheng, C.; Lei, M.; Feng, L.; Wong, T. L.; Ho, K. M.; Fung, K. K.; Loy, M. M. T.; Yu, D.; Wang, N. *ACS Nano* **2009**, *3*, 53–58.
- (5) Wang, Z.; Lin, C.; Liu, X.; Li, G.; Luo, Y.; Quan, Z.; Xiang, H.; Lin, J. *J. Phys. Chem. B* **2006**, *110*, 9469–9476.
- (6) Lin, D.; Wu, H.; Zhang, R.; Pan, W. *Chem. Mater.* **2009**, *21*, 3479–3484.
- (7) Lahiri, J.; Batzill, M. *J. Phys. Chem. C* **2008**, *112*, 4304–4307.
- (8) Maeda, K.; Takata, T.; Hara, M.; Saito, N.; Inoue, Y.; Kobayashi, H.; Domen, K. *J. Am. Chem. Soc.* **2005**, *127*, 8286–8287.
- (9) Su, Y. K.; Peng, S. M.; Ji, L. W.; Wu, C. Z.; Cheng, W. B.; Liu, C. H. *Langmuir* **2010**, *26*, 603–606.
- (10) Takanezawa, K.; Hirota, K.; Wei, Q.-S.; Tajima, K.; Hashimoto, K. *J. Phys. Chem. C* **2007**, *111*, 7218–7223.
- (11) Barick, K. C.; Aslam, M.; Dravid, V. P.; Bahadur, D. *J. Phys. Chem. C* **2008**, *112*, 15163–15170.
- (12) Strunskus, T.; Fuchs, O.; Weinhardt, L.; Heske, C.; Guraya, M.; Muhler, M.; Staemmler, V.; Woll, C. J. *Electron Spectrosc. Relat. Phenom.* **2004**, *134*, 183–189.
- (13) Spanhel, L.; Anderson, M. A. *J. Am. Chem. Soc.* **1991**, *113*, 2826–2833.
- (14) Sun, M.; Hao, W.; Wang, C.; Wang, T. *Chem. Phys. Lett.* **2007**, *443*, 342–346.
- (15) Wang, G.; Chen, D.; Zhang, H.; Zhang, J. Z.; Li, J. *J. Phys. Chem. C* **2008**, *112*, 8850–8855.
- (16) Liu, D.-P.; Li, G.-D.; Su, Y.; Chen, J.-S. *Angew. Chem., Int. Ed.* **2006**, *45*, 7370–7373.
- (17) Norberg, N. S.; Gamelin, D. R. *J. Phys. Chem. B* **2005**, *109*, 20810–20816.
- (18) Lee, W.; Jeong, M.-C.; Myoung, J.-M. *Acta Mater.* **2004**, *52*, 3949–3957.
- (19) Hartlieb, K. J.; Raston, C. L.; Saunders, M. *Chem. Mater.* **2007**, *19*, 5453–5459.
- (20) Amirav, L.; Amirav, A.; Lifshitz, E. *J. Phys. Chem. B* **2005**, *109*, 9857–9860.
- (21) Grassian, V. H., Ed. *Nanoscience and Nanotechnology; Environmental and Health Impacts*; John Wiley & Sons: New York, 2008.
- (22) Hassellöv, M.; Readman, J.; Ranville, J.; Tiede, K. *Ecotoxicology* **2008**, *17*, 344–361.
- (23) Prades, J. D.; Cirera, A.; Morante, J. R. *Sens. Actuators, B* **2009**, *142*, 179–184.
- (24) Oudar, J. *Catal. Rev.—Sci. Eng.* **1980**, *22*, 171–195.
- (25) Chaturvedi, S.; Rodriguez, J. A.; Jirsak, T.; Hrbek, J. *J. Phys. Chem. B* **1998**, *102*, 7033–7043.
- (26) Li, G.; Larsen, S. C.; Grassian, V. H. *J. Mol. Catal. A: Chem.* **2005**, *227*, 25–35.
- (27) Baltrusaitis, J.; Usher, C. R.; Grassian, V. H. *Phys. Chem. Chem. Phys.* **2007**, *9*, 3011–3024.
- (28) Fairley, N. *CasaXPS Version 2.3.14*, www.casaxps.com, 1999–2010.
- (29) Zhou, Z.; Deng, Y. *J. Phys. Chem. C* **2009**, *113*, 19853–19858.
- (30) Tokumoto, M. S.; Pulcinelli, S. H.; Santilli, C. V.; Briois, V. *J. Phys. Chem. B* **2003**, *107*, 568–574.
- (31) Patterson, A. L. *Phys. Rev.* **1939**, *56*, 978.
- (32) Shen, G.; Bando, Y.; Chen, D.; Liu, B.; Zhi, C.; Golberg, D. *J. Phys. Chem. B* **2006**, *110*, 3973–3978.
- (33) Yue, J.; Jiang, X.; Zeng, Q.; Yu, A. *Solid State Sci.* **2010**, *12*, 1152–1159.
- (34) Winterer, M. *Chem. Mater.* **2010**, *22*, 85–91.
- (35) Diaz Fleming, G.; Campos Vallette, M. M.; Clavijo, E.; Diez, S.; Saavedra, M. *Spectrochim. Acta, Part A* **1998**, *55*, 1827–1835.
- (36) Salavati-Niasari, M.; Davar, F.; Mazaheri, M. *Mater. Lett.* **2008**, *62*, 1890–1892.
- (37) Ismail, H. M. *J. Anal. Appl. Pyrolysis* **1991**, *21*, 315–326.
- (38) Nakamoto, K. *Infrared Spectra of Inorganic and Coordination Compounds*; Wiley: New York, 1970.
- (39) Berben, P. H.; Kappers, M. J.; Geus, J. W. *Microchim. Acta* **1988**, *95*, 15–18.
- (40) Thompson, M. M.; Palmer, R. A. *Appl. Spectrosc.* **1988**, *42*, 945–951.
- (41) Nakamoto, K.; Fujita, J.; Tanaka, S.; Kobayashi, M. *J. Am. Chem. Soc.* **1957**, *79*, 4904–4908.
- (42) Stark, J. V.; Park, D. G.; Lagadic, I.; Klabunde, K. J. *Chem. Mater.* **1996**, *8*, 1904–1912.
- (43) Lindberg, B. J.; Hamrin, K.; Johansson, G.; Gelius, U.; Fahlman, A.; Nordling, C.; Siegbahn, K. *Phys. Scr.* **1970**, *1*, 286–98.
- (44) Brion, D. *Appl. Surf. Sci.* **1980**, *5*, 133–52.
- (45) Riga, J.; Verbist, J. J. *J. Chem. Soc., Perkin Trans. 2* **1983**, 1545–51.
- (46) Li, J.; Shang, J.; Zhu, T. *Sci. China, Ser. B: Chem.* **2011**, *54*, 161–166.
- (47) Chan, S.; Barteau, M. *Top. Catal.* **2011**, 1–12.
- (48) Chan, S. C.; Barteau, M. A. *Langmuir* **2005**, *21*, 5588–5595.
- (49) Farneth, W. E.; McLean, R. S.; Bolt, J. D.; Dokou, E.; Barteau, M. A. *Langmuir* **1999**, *15*, 8569–8573.